Int. J. Electrochem. Sci., 17 **(2022)** Article Number: 220318, doi: 10.20964/2022.03.40

International Journal of
ELECTROCHEMICAL
SCIENCE
www.electrochemsci.org

Quick Evaluation of the State-of-Health of Spent Lithium-Ion Battery Modules

Huiqin Sun[1], Wei Liu[2], Zhichao Du[3], Xinzhou Li[1], Zaiguo Fu[1], Qiangqiang Liao[1,]*

[1] Shanghai Key Laboratory of Materials Protection and Advanced Materials in Electric Power, Shanghai Engineering Research Center of Electric Energy Conversion, Shanghai University of Electric Power, Shanghai 200090, China
[2] Electric Power Research Institute of Guizhou Power Grid Co., Ltd., Guiyang 550002, China
[3] Shanghai Electric Distributed Energy Technology company limited, Shanghai 201199, China
[*]E-mail: liaoqiangqiang@shiep.edu.cn

Received: 2 December 2021 / *Accepted:* 6 January 2022 / *Published:* 2 February 2022

A decommissioned battery module with 15 in parallel and 4 series from an electric vehicle was aged at 2 C-rate in the SOC range of 30–80% in the laboratory until its state of health (SOH) value reached about 60%. The module capacity was calibrated at 1/5 C-rate after every 100 or 200 cycles of aging. The probability density function (PDF) method and incremental capacity analysis (ICA) were introduced to establish an SOH model of battery modules against experimental charge and discharge voltage data in the process of capacity calibration. As a new SOH evaluation algorithm, the discrete Fréchet distance was also proposed for the battery module, and the concept of mean Fréchet distance (MFD) was given as a quick evaluation index of the module's SOH. The results showed that there was a fine negative linear dependence of module SOH on MFD. The discrete Fréchet distance method has better accuracy than ICA and PDF in terms of module SOH evaluation.

Keywords: retired battery modules; SOH evaluation; incremental capacity analysis; probability density function; discrete Fréchet distance

1. INTRODUCTION

China's government has promised to achieve peak carbon emissions by 2030 and to accomplish carbon neutralization by 2060 under the framework of the Paris Climate Accord. EV instead of fuel vehicle is one of the most important ways to achieve carbon neutral target. The number of EVs in China reached 4.92 million by the end of 2020 thanks to the strong support of the Chinese government's electric vehicle policy and the rapid development of high-performance and low-cost lithium-ion battery technology [1]. Repeated charging and discharging of EVs will lead to constant attenuation of battery capacity [2]. It is generally believed that when the battery SOH value of an EV attenuates to below 80%

it still needs to be retired from the EV due to the concerns of battery safety, mileage anxiety, and frequent charging although it is not spoiled [3]. Despite EV battery retirement, it is still feasible for them to carry out mild charging and discharging in a static indoor environment with suitable temperature [4]. Distributed industrial park or household energy storage is a suitable scene for the spent battery reuse served as renewable energy storage [5], demand response services [6], backup power [7] and so on. However, the inconsistency of retired batteries of EVs is very significant [8]. The premise of decommissioned batteries as energy storage systems is that there should be good consistency among them; otherwise, the capacity of the energy storage system composed of inconsistent batteries will be greatly reduced due to the bucket effect. The residual capacity or SOH value is an important indicator of the consistency of retired batteries [9,10]. It is technically mature that the residual capacity of decommissioned batteries is detected by traditional capacity calibration methods [11–16], but they are time consuming and energy consuming. After all, the advantage of retired batteries in energy storage systems is their low cost compared with new batteries [17]. If traditional capacity calibration methods are used for the consistent sorting of retired batteries, the energy storage system composed of them will not be economical. Therefore, the establishment of a quick and accurate battery SOH evaluation method is one of the key technologies to achieve low-cost echelon utilization of retired batteries.

There has been abundant research on quick evaluation methods of battery SOH in the literature in recent years. The general idea is to set up a quantitative battery SOH model with battery performance parameters that can be quickly detected by a certain algorithm, such as internal resistance, voltage, and temperature, so as to accomplish rapid SOH evaluation. Dattu et al. [18] compared two different and simplified prismatic 20 Ah $LiFePO_4$ cell models at different current rates and cooling water temperatures, namely the Lumped Li-ion model, suggesting that the Lumped model could replace the Li-ion model at less than 2 C-rate for rudimentary examination of the design of battery thermal management systems. Tran et al. [19,20] predicted the thermal and electrical behaviors of Li-ion cells using four machine learning regression models—k-nearest neighbors, linear regression, random forest, and decision tree—in which the decision-tree-based model was the best model. Duan et al. [21] believed that the channel breadth of cooling plates has a large impact on the battery module temperature. A temperature control strategy has been found to guarantee that the battery pack can work within the optimal temperature region under different discharge depths. Gargh et al. [22] found that a lithium-ion battery was susceptible to lithium plating at a fast-charging rate of more than 3 C-rate, and there was a linear capacity loss relationship with an impedance change in the plated batteries. Wang et al. [23] put forward a charge-transfer resistance model based on temperature and SOC to evaluate battery SOH; although, the error was large in the case of high SOC and temperature. Our research group found that concentration polarization impedance had a large influence on the available capacity of retired batteries, and the lithium-ion diffusion coefficient converted from concentration polarization impedance was used as a quick assessment index of battery SOH [8]. As it should be, on the basis of the change in internal resistance, the battery SOH model is an off-line rapid evaluation model because the on-line examination function of battery internal resistance is not available in most commercial battery management systems. Therefore, many researchers regard the SOC or the capacity, voltage, and temperature detected online by battery management systems as the basic parameters of battery SOH evaluation and achieve online evaluation of SOH values through modeling. There are many publications showing that the peak

parameters on incremental capacity curves strongly correlate with battery SOH [24–26]. Considering that the actual operation of the battery system is not complete charge and discharge, Tang et al. [27] collected charging curve data in the middle SOC range and proposed a concept of regional capacity, linearly positively correlated with SOH. The change in open-circuit voltage and working voltage can also reflect the SOH of the battery. Baghdadi et al. [28] discovered that battery SOH was linearly dependent on the open-circuit potential (OCP) of the fully charged battery after a break of 30 min. Our research group found that the battery module SOH had a negative linear correlation with the OCP range (ΔOCP) among cells in the module under a certain low SOC value [5]. The shortcoming of quick assessment methods based on OCP is that OCP stability takes a long time, and the same SOC value is needful for the OCP comparison of batteries. Feng et al. [29] employed the probability density function (PDF) method to process the working voltage data in the charge/discharge processes and proposed the integrated frequency of the voltage within a specific integration threshold as the characteristic index of SOH. The advantage of PDF is that it avoids the artificial setting of differential voltage (ΔV) in incremental capacity analysis (ICA). Besides the research of extracting an eigenvalue from single factor as SOH evaluation index, there are many articles to establish SOH evaluation models including two or more factors, such as capacity, voltage, temperature, and internal resistance [30–32]. If more SOH-influencing factors are involved, without doubt, the corresponding algorithm and model will be more complex.

In addition, a module is composed of cells by welding, while a system is composed of modules by riveting. Module disassembly from a pack is easy and the cells are not easily damaged, while cell disassembly from a module is more difficult and the cells are apt to be spoiled. The quick evaluation, sorting, and grouping of batteries from the perspective of modules are more conducive to the low-cost utilization of retired batteries.

From a review of the literature, it is clear that there are still few reports on accurate and rapid SOH evaluation methods of battery modules [5,26,33]. Accordingly, the novelty of our work is that a quick evaluation model for battery module SOH is proposed using the discrete Fréchet distance method, which is more accurate than that obtained from ICA and PDF methods. Besides the introduction, the remainder of the paper is arranged as follows: section 2 describes the battery module, experimental instrument, and specific analysis methods. The results and discussion are given in section 3, while the conclusions are presented in section 4.

2. EXPERIMENTAL

2.1 Battery module

An $LiFePO_4$ battery module (15 in parallel and 4 series, 15P4S for short) with a rated capacity of 40 Ah was decommissioned from a Chery S18B EV and used in the test (Fig. 1). The module composed of four 15P1S bricks in series was manufactured by Tianjin Bic Battery Co., Ltd., China. The positive material of the battery cell was lithium iron phosphate, while its negative material was graphite. The current collectors of the negative and positive electrodes were copper foil and aluminum foil,

respectively. The electrolyte salt of the battery was 1 mol/L^{-1} $LiPF_6$, and the electrolyte solvent was composed of diethyl carbonate, vinyl carbonate, and methyl ethyl carbonate in a ratio of 1:1:1. The nominal capacity and voltage of one battery in the module was 2.69 Ah and 3.2 V, respectively. Since it had served in the EV for more than three years, the module capacity was calibrated before the aging test. Section 2.3.2 provides details on the capacity calibration process, and the initial capacity of the retired module was 37.88 Ah, i.e., 94.7% SOH [2].

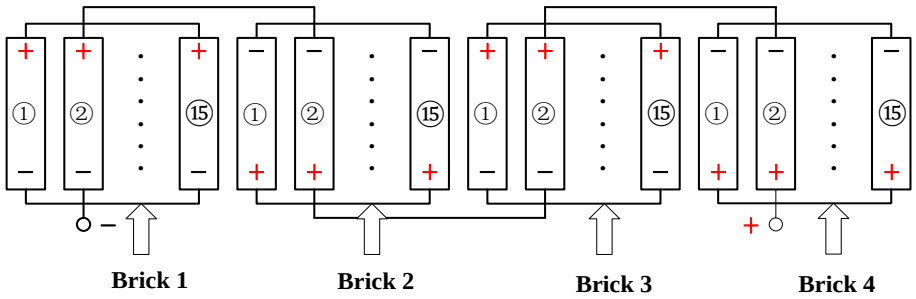

Figure 1. Series parallel structure diagram of the 15P4S module.

2.2 Experimental instrument

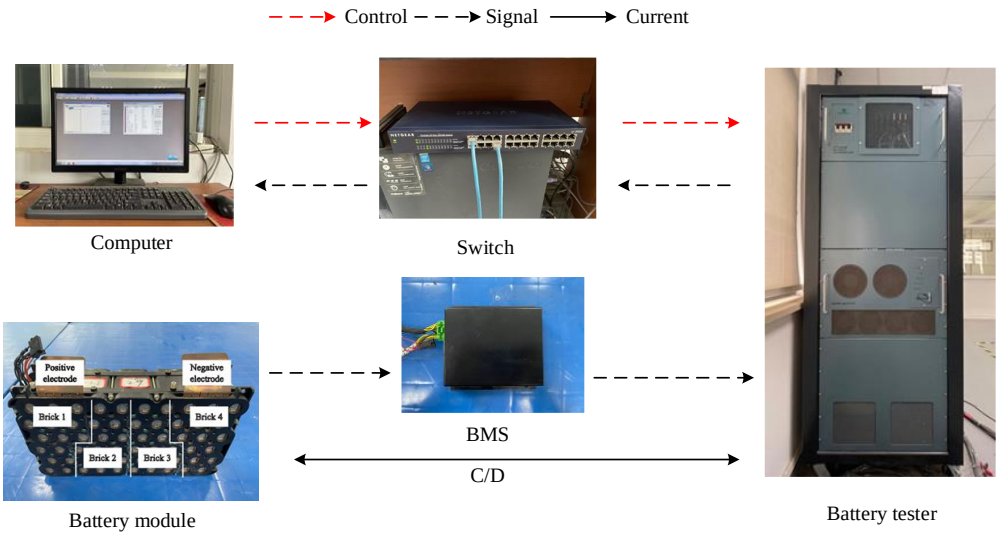

Figure 2. Picture of the experimental setup.

Fig. 2 shows the actual picture of the experimental setup. The battery test platform consisted of a battery tester (Bitrode FTV 1-300-100, USA), data converter machine (Netgear JFS524, USA), data line (Blekin Co., Ltd., China), battery management system (BMS) (Shanghai Qiansai electronics Co., Ltd., China), and central control computer (Lenovo Yangtian T4900V-00, China). The battery tester was responsible for the module charge/discharge, while the BMS surveyed battery parameters such as current with 1 mA accuracy, voltage with 1 mV accuracy, temperature, and so on. A J-type thermocouple (accuracy of 0.5°C) was used for the battery surface temperature test. The computer was in charge of the

programming and operation of charge–discharge protocols and the recording and storage of test data, while the data converter machine and the data line administered data transfer.

2.3 Test methods

2.3.1 Capacity calibration

The module was discharged at an invariable 1/5 C-rate (8A) until a module potential of 10.8 V or a cell potential of 2.5 V was attained. After standing for 30 min, it was charged at 1/5 C-rate until a module potential of 14.6 V (3.65 V × 4) or a cell potential of 3.75 V was achieved, and then it was transferred to an invariable potential phase until the current was less than 1/30 C (1.3 A). At last, it was discharged at 1/5 C-rate until a module potential of 10.8 V or a cell potential of 2.5 V was reached after a break of 30 min [16]. This is the calibrated discharge capacity, C_{dis}. All battery aging tests and capacity calibration tests were conducted at ambient temperature (25±1°C).

2.3.2 Module aging

The aging protocol of the module was set to invariable 2 C-rate (80 A) charge–discharge in the range of 30–80% SOC in order to simulate the energy storage application scenarios of high rate and shallow charge–discharge. First, the module was discharged at an invariable 1/5 C-rate (8 A) until the module potential reached 10.8 V (2.7 V × 4) or the cell voltage reached 2.5 V. Next, it was charged to 80% SOC with 2 C-rate until the step time T_1 was achieved. Then, it was discharged to 30% SOC with 2 C-rate until the step time T_2 ended. Finally, the module stopped after the charging time was T_3. The module should stand for 30 min every charging and discharging interval. It went back and forth in the range of 30–80% SOC. The step times of $T_1 = C_{dis} \times 0.8/80$ (h), $T_2 = C_{dis} \times 0.5/80$ (h), and $T_3 = C_{dis} \times 0.5/80$ (h) were calculated, where C_{dis} is the discharge capacity calibrated.

The module was aged at 2 C-rate in the SOC range of 30–80% until its SOH was about 60%. The module capacity was calibrated every 100 cycles in the first 600 cycles and every 200 cycles afterwards. The calibration was more frequent at the early aging stage than at the later stage because the decay rate of the module was not known at the early stage of aging.

2.4 Analysis methods

2.4.1 ICA method

The ICA method transforms the voltage platform of a battery on the general charge–discharge potential curve into ΔQ / ΔV peaks, which could be obviously identified on the ICA curve [25]. The ICA curve describes the dependence of the ΔQ / ΔV value in a fixed voltage range on the battery charge or discharge voltage. Because the ICA curve is more sensitive than the general charge–discharge curve, some important characteristic electrochemical information of the battery can be obtained by identifying

the progress of these ΔQ / ΔV peaks with the changes in the environment, working conditions, and different health states. After that, the dependence of the internal and external electrochemical parameters of the battery can be established. In the article, the charge–discharge curve was converted into an ICA curve by differential processing and locally weighted scatterplot smoothing using Origin software. The voltage range took the fixed value of ΔV= 2 mV, and the points of windows were set to 80.

2.4.2 PDF method

The PDF is a function describing the possibility of the output value of continuous random variable near a certain value point. The loss of electrode active materials and recyclable lithium is considered to be the main factor of battery aging. The charge–discharge plateau becomes shorter with the increase in the degree of aging. The PDF method is used to count the frequency of voltage values on the platform of the charge–discharge curve. The frequency of some characteristic voltage values (i.e., probability density) can reflect the degree of battery aging. In this paper, PDF processing of charge–discharge voltage data was accomplished using the *ksdensity* function in MATLAB software [29].

2.4.3 Discrete Fréchet distance

The Fréchet distance is usually used to estimate the similarity of two continuous curves, $\mathrm{A\ and\ B}:[0,1]\rightarrow R^2$, on Fréchet space, where R^2 is the metric space [34,35]. Eiter et al. [36] defined the discrete Fréchet distance based on the continuous Fréchet distance in order to better solve practical problems. In this paper, the discrete Fréchet distance method was used to judge the similarity of charging and discharging curves of series cells in a battery module. On this basis, the mean Fréchet distance (MFD) is proposed as the characteristic index of the quick evaluation of battery module SOH. The calculation process of the MFD value is as follows.

The voltage–time series set comes from the BMS. Curve A:$[0, m]\rightarrow R^2$ denotes the mean voltage curve of charge or discharge among cells in a module at a certain current rate in the last m minutes. Set $\sigma(A) = (a_1, a_2, \ldots, a_m)$ represents the voltage data set of the same time series in Curve A, in which m is the sampling period and the sampling time point is fixed to the m-th, *(m-1)*-th, *(m-2)*-th, …, *3*rd, *2*nd, *1*st minute. In the same way, Curve B:$[0, m]\rightarrow R^2$ denotes the charge or discharge voltage curve of a certain cell in the module at the same current rate in the last m minutes. Set $\sigma(B) = (b_1, b_2, \ldots, b_m)$ indicates the voltage data set of the same time series in Curve B. In addition, $d(a_i, b_j) = a_i - b_j$ signifies the connection distance between element a_i in Set $\sigma(A)$ and element b_j in Set $\sigma(B)$, while $\partial_{dF}(i, j)$ symbolizes the discrete Fréchet distance when two particles move to the i position of Curve A and the j position of Curve B, respectively.

The element connection matrix, $D_{a\times b}$, of Curves A and B is calculated from Sets $\sigma(A)$ and $\sigma(B)$ by Eqs. (1)–(4), as follows:

$$D_{a\times b}=\begin{bmatrix} d(1,1) & \cdots & d(1,m) \\ \vdots & \ddots & \vdots \\ d(m,1) & \cdots & d(m,m) \end{bmatrix} \quad (1)$$

Let $i = 1$ and $j = 1$, then $\partial_{dF}(1, 1) = d(a_1, b_1)$ (2)

Let $i = 2 \to m$ and $j = 1$, then $\partial_{dF}(i, j) = \max\left\{\partial_{dF}(i-1, j), d(a_i, b_j)\right\}$ (3)

Let $i = 1$ and $j = 2 \to m$, then $\partial_{dF}(i, j) = \max\left\{\partial_{dF}(i, j-1), d(a_i, b_j)\right\}$ (4)

Starting from $i = 2$ and $j = 2$, search forward according to Eq. (5) until $i = m$ and $j = m$. Then, the discrete Fréchet distance between Curves *A* and *B* equals $\partial_{dF}(m, m)$, i.e., $\partial_{dF}(A, B) = \partial_{dF}(m, m)$。.

$$\begin{cases} \partial_{dF}(i,j) = max\{\partial', d(a_i, b_j)\} \\ \partial' = min\{\partial_{dF}(i-1,j), \partial_{dF}(i-1,j-1), \partial_{dF}(i,j-1)\} \end{cases} \quad (5)$$

The $\partial_{dF}(A, B)$ value indicates the degree of "shape similarity" of a curve. The smaller the $\partial_{dF}(A, B)$ value, the more similar the curve is. The battery in this test was a 15P4S module. The BMS can collect four sets of cell voltages during the charging and discharging process of the module. If the discrete Fréchet distances between the voltage curves (B_1, B_2, B_3, and B_4) of four cells and the mean voltage curve (A) of the module are respectively defined as $\partial_{dF}(A, B_1)$, $\partial_{dF}(A, B_2)$, $\partial_{dF}(A, B_3)$, and $\partial_{dF}(A, B_4)$, then the mean Fréchet distance (*MFD*) of the module is calculated according to Eq. (6). The smaller the *MFD* value, the larger the module SOH.

$$MFD = \frac{1}{4}\sum_{n=1}^{4}\partial(A, B_n) \quad (6)$$

3. RESULTS AND DISCUSSION

3.1 Cycling degradation of a 15P4S module

The 15P4S module completed 3800 cycles of charging and discharging after its SOH decreased from 94.7% to 61% at 2 C-rate in the range of 30–80% SOC at 25±1°C ambient temperature.

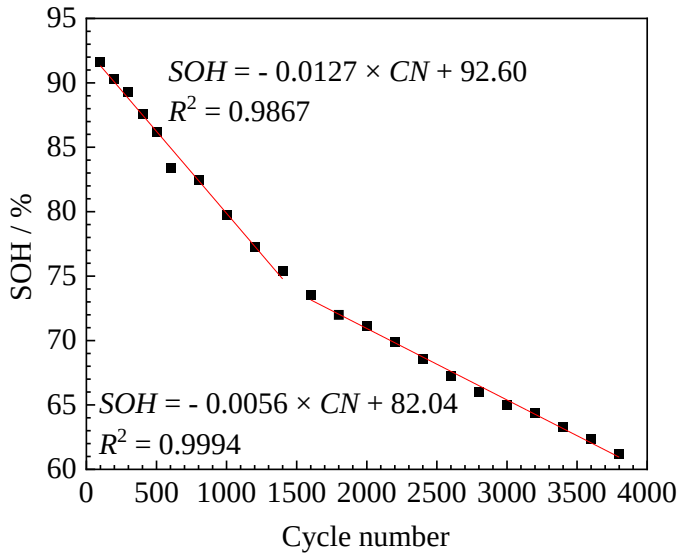

Figure 3. The SOH dependence of the 15P4S module on the cycle number at 2 C-rate charge–discharge in the range of 30–80% SOC at 25±1°C ambient temperature.

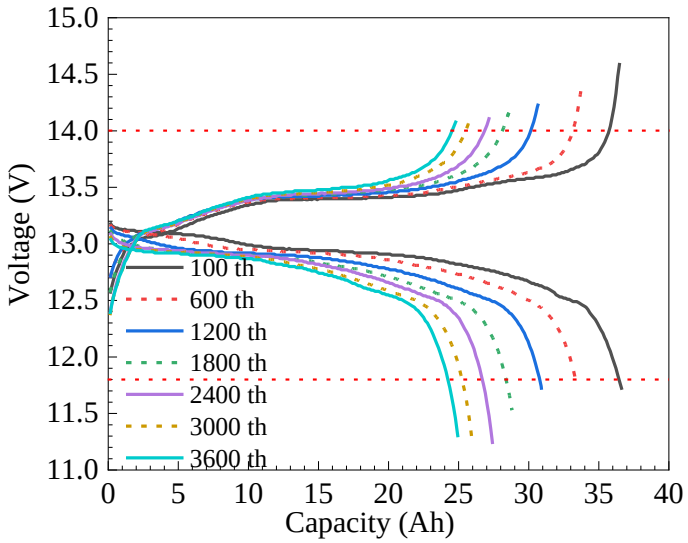

Figure 4. Charge–discharge curves of the 15P4S module during the capacity calibration process at 1/5 C-rate after different aging cycles.

A total charge of 827.1 kWh, a discharge of 702.9 kWh, and an energy conversion efficiency of 84.99% were achieved during the whole aging process. Fig. 3 illustrates the SOH dependence of the 15P4S module on cycle number (CN), suggesting that the aging of the module shows a trend from fast to slow in this aging mode. Piecewise linear relationships between SOH and CN in different CN ranges are expressed by Eq. (7), whose *R*-squared is more than 0.986, showing high goodness of fit.

$$\begin{cases} SOH = -0.0127 \times CN + 92.60, R^2 = 0.9867, CN \in [0,1400] \\ SOH = -0.0056 \times CN + 82.04, R^2 = 0.9994, CN \in [1500,3800] \end{cases} \quad (7)$$

Fig. 4 illustrates the charge–discharge curves of the 15P4S module during the capacity calibration process at 1/5 C-rate after different aging cycles. It can be seen from Fig. 4 that the module charge–discharge platforms become shorter with the increase in aging cycle, showing that the module SOH gets smaller. The voltage plateau of the charge curve increases with the increase in aging cycle, while that of the discharge curve decreases, indicating that aging leads to an increase in battery internal resistance.

3.2 Incremental capacity analysis

Fig. 5 shows the incremental capacity curves (a) of the 15P4S module during the capacity calibration process at 1/5 C-rate after different aging cycles and its $H_{\text{ICA-C}} - SOH$ (b) and $H_{\text{ICA-D}} - SOH$ (c) models. As shown in Fig. 5(a), there are three peaks of C_1, C_2, and C_3 in the incremental capacity curve of charge at 13.08 V, 13.41 V, and 13.57 V, respectively, at the 100th cycle, while three peaks of D_1, D_2, and D_3 also appear in the incremental capacity curve of discharge at 12.54 V, 12.93 V, and 13.09 V, respectively. For the $LiFePO_4$ cathode, the conversion between $FePO_4$ and $LiFePO_4$ occurs during the process of charging and discharging, which can be divided into two stages. One is the non-stoichiometric solid solution phase in the single-phase region at the beginning and end of charge–discharge, while the other is the middle pseudo-binary phase transition between Li_xFePO_4 and $Li_{1-y}FePO_4$ [37,38], which contributes most of the capacity change in the battery voltage platform. For the graphite anode, at least five different stages of electrochemical reaction are accomplished for lithium ion intercalating into graphite to convert C_6 into LiC_6 during the charging process. The phenomenon is opposite in the process of discharge. If the charge–discharge current is very small and no more than 1/20 C, at least five different capacity increment peaks should appear in the incremental capacity curve, corresponding to the transformation of different lithium carbides in five reaction stages [38]. Since the current rate is 1/5 C-rate, there are only three peaks in the incremental capacity curves in Fig. 3, whether in the charging or discharging process, corresponding to the transformation between C_6, the lithium carbide intermediate state (LiC_x, x=72, 36, 18, 12, etc.), and LiC_6 [39]. The heights of six peaks in Fig. 5 have a tendency to decrease with the aging evolution, and even the peaks of C_3 and D_3 gradually disappear. In particular, the peaks of C_2 and D_2 decreased most obviously. Therefore, the peak height of C_2 and D_2 is taken as the characteristic index of SOH evaluation, and the quantitative model between them is established. Figs. 5(b) and (c) display the SOH dependence of the 15P4S module on the peak heights of C_2 and D_2, respectively, in which the $H_{\text{ICA-C}}$ and $H_{\text{ICA-D}}$ values refer to the peak heights of C_2 and D_2, respectively. The results show that there is a good linear positive correlation between module SOH and $H_{\text{ICA-C}}$ or $H_{\text{ICA-D}}$ in charging or discharging processes, with an *R*-squared of more than 0.91.

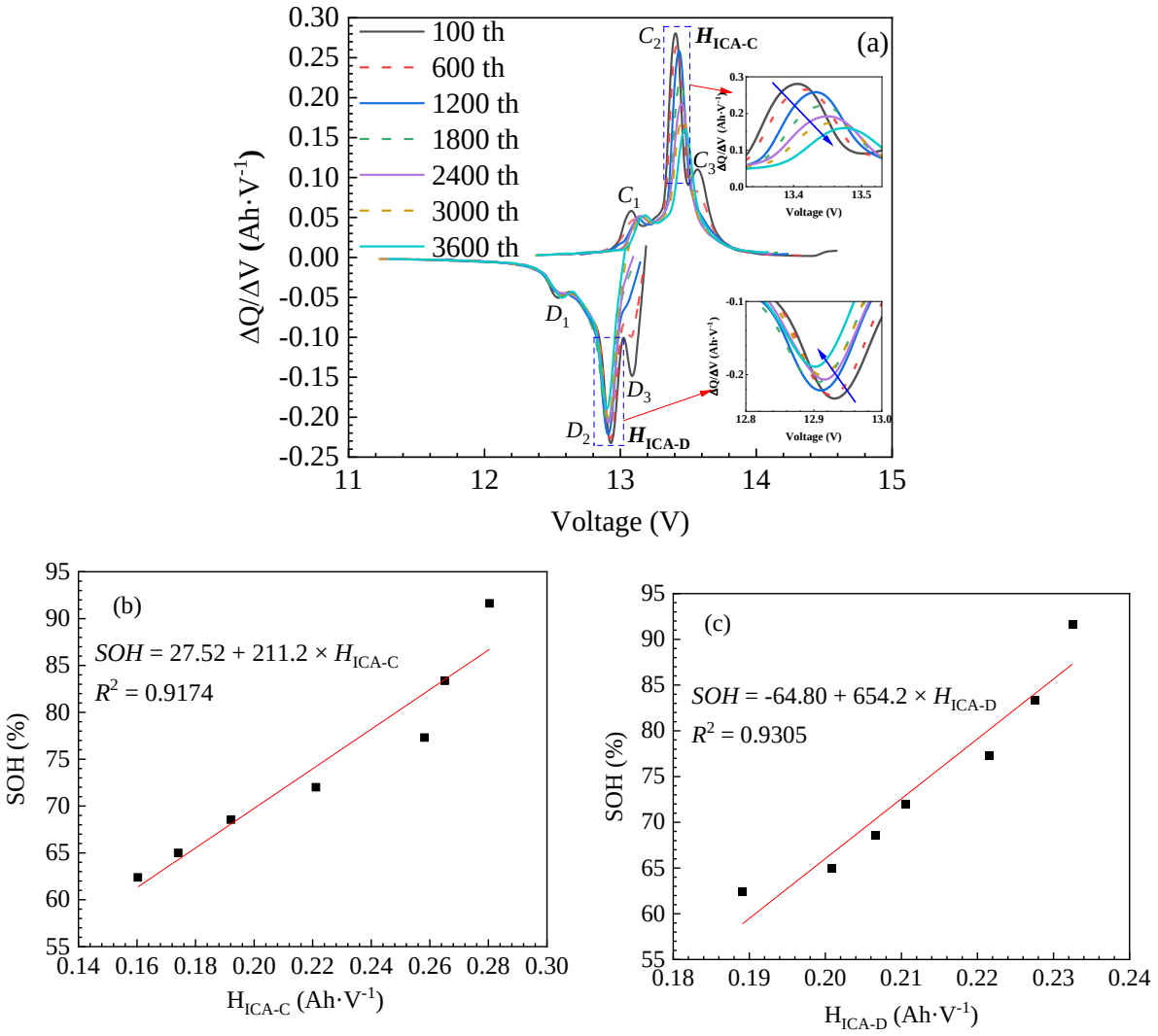

Figure 5. Incremental capacity curves (a) of the 15P4S module during the capacity calibration process at 1/5 C-rate after different aging cycles and its $H_{\text{ICA-C}} - SOH$ (b) and $H_{\text{ICA-D}} - SOH$ (c) models.

3.3 Analysis of probability density function

The equivalence between incremental capacity analysis and probability density function has been discussed in detail in the literature [29]. Therefore, the meanings of the peaks in the probability density function curve are the same as those in the incremental capacity curve, which will not be discussed here. Fig. 6 illustrates the probability density curves (a) of the 15P4S module converted from all the voltage data in Fig. 4 and its $H_{\text{PDF-C}} - SOH$ (b) and $H_{\text{PDF-D}} - SOH$ (c) models, in which the $H_{\text{PDF-C}}$ and $H_{\text{PDF-D}}$ values signify the maximum peak heights of probability density curves in the process of charging and discharging, respectively. Figs. 6(b) and (c) show that there is a good linear relationship between the peak height and SOH in the charging process, while the linear relationship is not good in the discharging process. Moreover, the goodness of fit of the two SOH models is not as good as that from the incremental capacity curves. Because PDF describes the possibility of the output value of continuous random variable near a certain value point, the probability density of a certain value should be compared in the same data

interval. For example, the probability density of 5 apples in 100 fruits is obviously different from that of 5 apples in 150 fruits. The end-of-charge voltage in the charging process of the module is often different with the increase in cycle number due to the inconsistency among the cells in the retired battery module, as shown in Fig. 4. The same is true in the discharge process. Therefore, the voltage data in the same voltage range is extracted and transformed into probability density. Fig. 7 shows the probability density curves (a) of the 15P4S module converted from the voltage data in the range of 11.8–14.0 V in Fig. 4 and its $H'_{\text{PDF-C}} - SOH$ (b) and $H'_{\text{PDF-D}} - SOH$ (c) models. It can be seen from Figs. 7(b) and (c) that the linear relationships between the peak height and SOH are significantly improved whether it is charging or discharging. Consequently, the premise of establishing a quick SOH evaluation model for retired battery modules by the PDF method is not only the same charge–discharge current rate [29] but also the same voltage range.

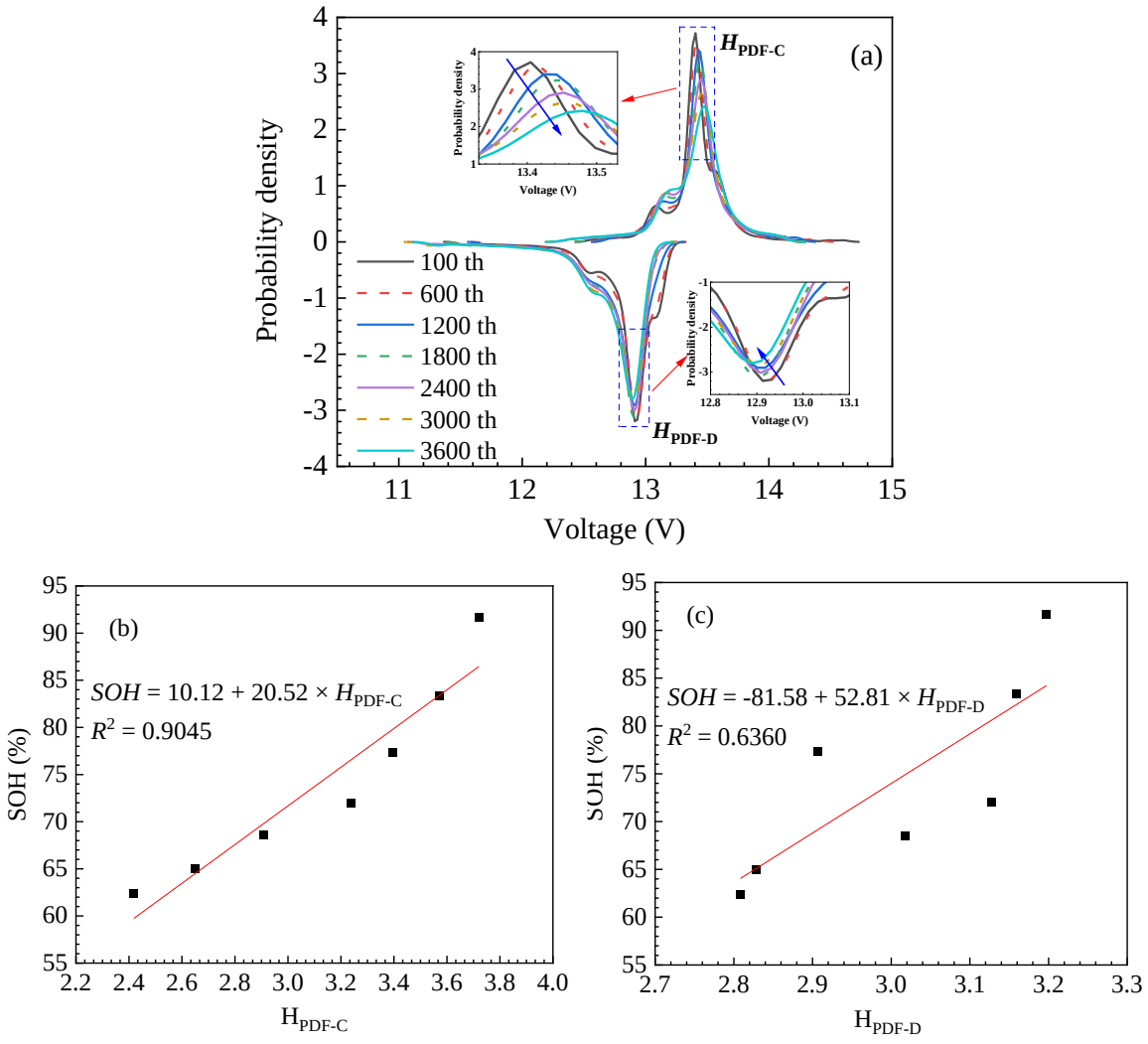

Figure 6. Probability density curves (a) of the 15P4S module converted from all the voltage data in Fig. 4 and its $H_{\text{PDF-C}} - SOH$ (b) and $H_{\text{PDF-D}} - SOH$ (c) models.

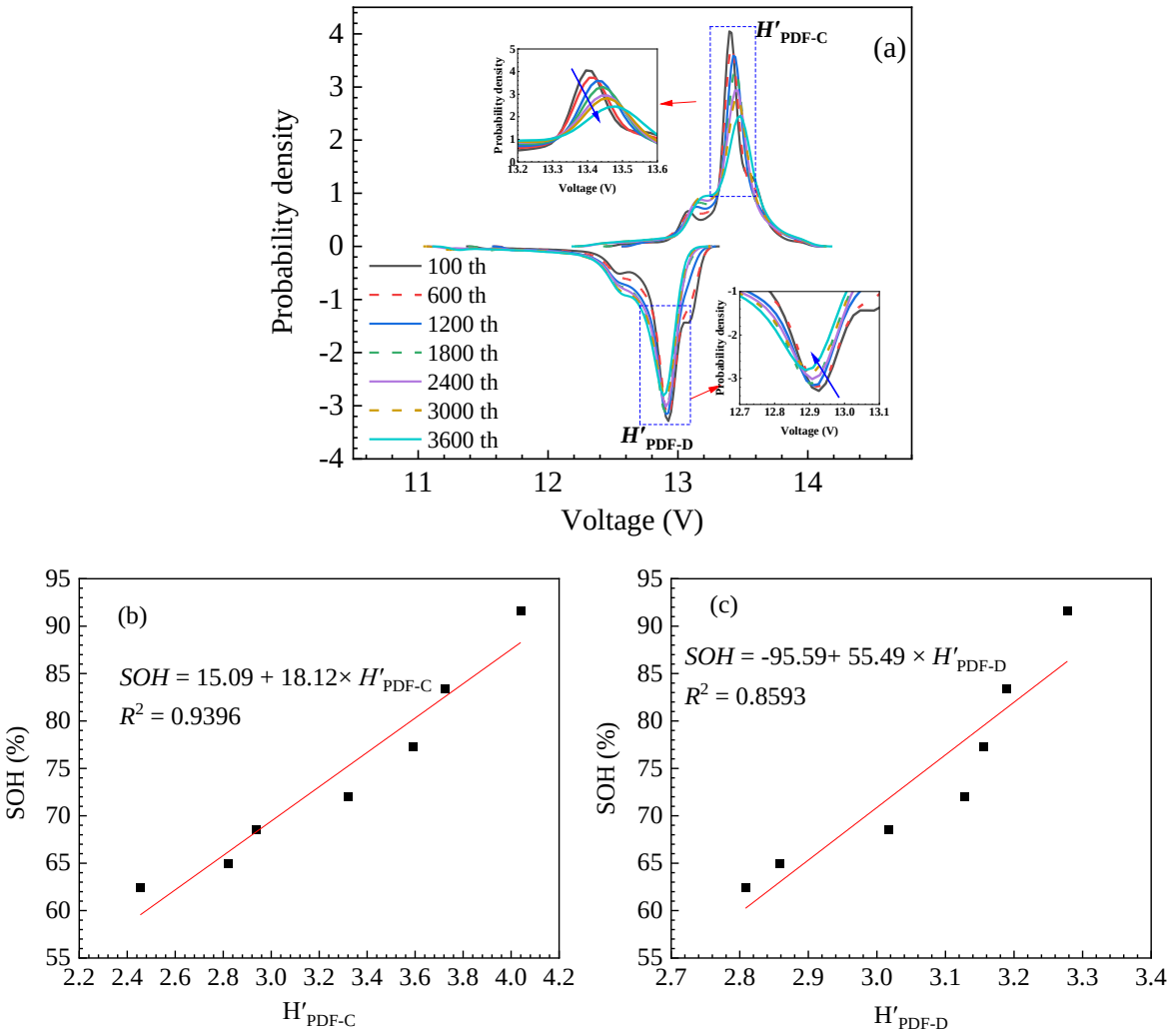

Figure 7. Probability density curves (a) of the 15P4S module converted from the voltage data in the range of 11.8–14.0 V in Fig. 4 and its $H'_{PDF\text{-}C} - SOH$ (b) and $H'_{PDF\text{-}D} - SOH$ (c) models.

3.4 Analysis of discrete Fréchet distance

Fig. 8 presents a three-dimensional diagram of charging time, MFD, and SOH, in which the charging time is counted down from the end of charging. In Fig. 8, the 0 min starting point of each curve at the left of the abscissa actually represents the time that the battery is full, while the end time of this curve at the right of the abscissa represents the time that the battery just starts charging. The smaller the module SOH, the shorter the charging time. In order to display the MFD values of the fully charged modules with different SOH values on the side planes of the three-dimensional graph, the charging time of abscissa is expressed in the form of count backwards from the charging end. It can be seen from Fig. 8 that there is a large difference among the cells in the module at the beginning and end of charging for a module with a specific SOH value, which leads to a large MFD value of the module. The MFD value of the module increases with the decrease in SOH value at the end of charging for battery modules with different SOH values.

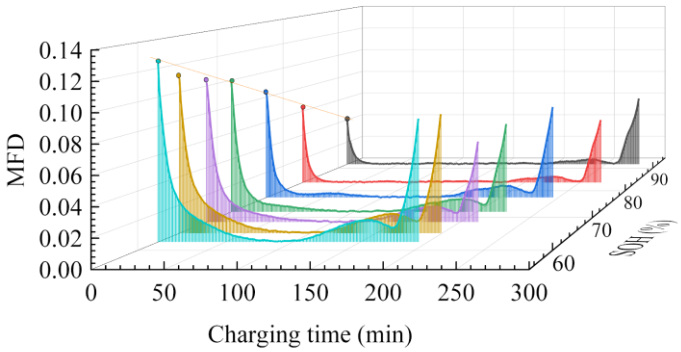

Figure 8. Three-dimensional diagram of charging time, MFD, and SOH, in which the charging time is counted down from the end of charging.

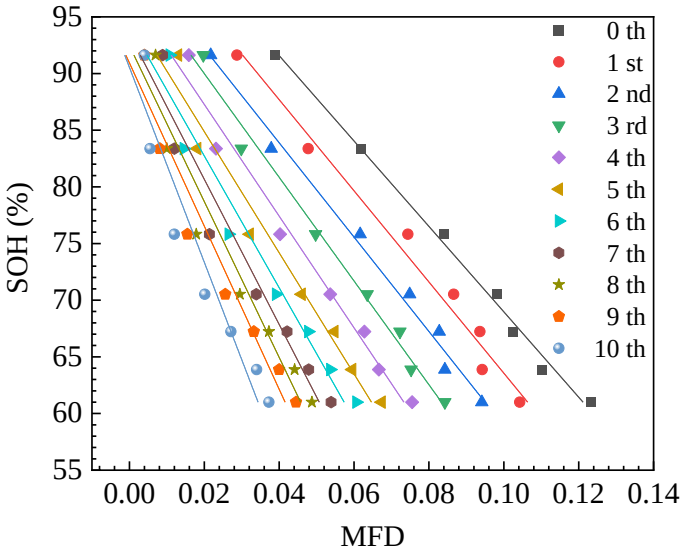

Figure 9. The SOH dependence of the module on MFD at different charging moments from the 0th to the 10th minute, counted down from the end of charging.

Table 1. MFD-SOH models at the charge terminals.

time (minute)	*MFD-SOH* model	R^2
0th	$SOH = 106.4 - 374.5\ MFD$	0.9939
1st	$SOH = 103.2 - 394.6\ MFD$	0.9772
2nd	$SOH = 100.2 - 411.7\ MFD$	0.9868
3rd	$SOH = 98.82 - 451.8\ MFD$	0.9873
4th	$SOH = 96.64 - 482.6\ MFD$	0.9792
5th	$SOH = 94.83 - 516.8\ MFD$	0.9667
6th	$SOH = 93.42 - 555.5\ MFD$	0.9550
7th	$SOH = 92.34 - 604.3\ MFD$	0.9436
8th	$SOH = 91.23 - 643.7\ MFD$	0.936
9th	$SOH = 89.97 - 680.2\ MFD$	0.9447
10th	$SOH = 89.12 - 788.5\ MFD$	0.9171

Fig. 9 displays the SOH dependence of the module on MFD at different charging moments from the 0th to the 10th minute, counted down from the end of charging, suggesting that there is a good linear negative correlation between MFD and the module SOH. Table 1 lists the MFD-SOH models at the charge terminal, demonstrating that the *R*-squared of the MFD-SOH model at the end of full charge (the 0th minute) is the largest, reaching 0.9939. The *R*-squared of MFD-SOH models decreased in general with time from the 0th to the 10th minute, counted down from the end of charging. The decrease in the *R*-squared with the countdown time means that the accuracy of SOH estimation becomes worse. However, the *R*-squared of the model at the 10th minute is still as high as 0.9171.

3.5 Comparison of three quick evaluation methods for module SOH

Fig. 10 shows the distribution of measured and evaluated SOH values by different models, in which the SOH_{MFD} and Err_{MFD} values are counted in light of the MFD-SOH model at the 0th minute. Table 2 lists the SOH values and relative errors obtained by different evaluation models, in which relative errors are calculated by Eq. (8). Comparing the maximum relative errors of SOH values evaluated by these five models, it was found that the MFD model was the smallest and the PDF-D model was the largest. The MFD model showed the best evaluation accuracy in these five models, and its maximum relative error was less than 2.5%. The absolute values of the relative errors of different SOH evaluation methods have been compared through literature searches. Table 3 shows the comparison of the absolute values of the relative errors of different methods in the literature. In the references mentioned above, SOH evaluation of different types of batteries by different methods at diverse charge–discharge rates has been reported. It can be seen from Table 3 that the absolute value of relative errors from the MFD method is the lowest.

$$\text{Err}\ (\%) = \frac{SOH_{Evaluated} - SOH_{Measured}}{SOH_{Measured}} \times 100 \qquad (8)$$

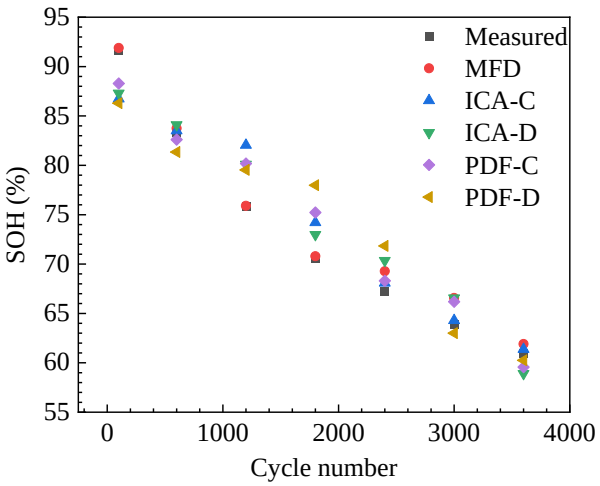

Figure 10. Distribution of measured and evaluated SOH values by different models.

Table 2. SOH values and relative errors obtained by different evaluation models.

Cycle number	100th	600th	1200th	1800th	2400th	3000th	3600th
Measured *SOH* (%)	91.63	83.38	77.30	72.01	68.55	65.00	62.38
SOH_{MFD} (%) / Err_{MFD} (%)	91.89/0.28	83.74/0.44	75.90/–1.81	70.79/–1.68	69.28/1.07	66.57/2.42	61.91/0.75
$SOH_{ICA\text{-}C}$ (%) / $Err_{ICA\text{-}C}$ (%)	86.74/–5.34	83.51/0.16	82.05/6.14	74.22/3.08	68.09/–0.67	64.29/–1.09	61.38/1.60
$SOH_{ICA\text{-}D}$ (%) / $Err_{ICA\text{-}D}$ (%)	87.30/–4.73	84.10/0.86	80.11/3.64	72.97/1.35	70.36/2.64	66.56/2.40	58.91/–5.56
$SOH_{PDF\text{-}C}$ (%) / $Err_{PDF\text{-}C}$ (%)	88.29/–3.65	82.60/–0.94	80.18/3.73	75.22/4.47	68.30/–0.36	66.18/1.82	59.57/–4.50
$SOH_{PDF\text{-}D}$ (%) / $Err_{PDF\text{-}D}$ (%)	86.30/–5.82	81.35/–2.43	79.54/2.90	77.98/8.31	71.83/4.78	63.00/–3.08	60.25/–3.41

Table 3. Comparison of the absolute value of the relative errors of different methods in the literature.

Method	Battery type	Current rate	Absolute value of relative error	Reference
MFD	$LiFePO_4$ batteries	1/5 C	Less than 2.5%	This work
Electrochemical impedance spectroscopy	$LiFePO_4$ batteries	2–20 C	Less than 4.2%	[40]
Neural network algorithm	$LiNiCoMnO_2$ batteries	1/3 C	Less than 4%	[41]
Dynamic impedance technique	$LiNiCoAlO_2$ batteries	Unspecified	Less than 5%	[42]
Dynamic Bayesian networks	$LiMn_2O_4$ batteries	1 C	Less than 5%	[43]
Wavelet analysis	$LiNiCoMnO_2$ batteries	1/2 C	Less than 5%	[44]

The advantage of ICA and PDF methods is that they only need module voltages rather than cell voltages. However, the differential voltage in the ICA method is artificially selected, and the incremental capacity curve needs to be smoothed. Module SOH evaluation by PDF needs to be based on the same current rate and voltage range in which the selection of voltage range is artificial. These treatments may be the causes of evaluation error. Besides, the LFP module consists of four 15P1S bricks in series, and the total voltage of the LFP module is equal to the sum of four bricks. The maximum peak height as a health factor in the ICA or PDF method is extracted from the total charging or discharging voltage of the whole module, not from the charging or discharging voltage of the "short-board" brick. In order to explore the influence of inconsistency among four batteries within the module on the SOH of the module, the discrete Fréchet distance method is used to judge the similarity of charging and discharging curves of series bricks in a battery module in the paper. On this basis, the MFD is proposed as the characteristic index of quick evaluation of battery module SOH. After considering the influence of the inconsistency on the SOH estimation, the discrete Fréchet distance method has better accuracy in SOH modeling than ICA or the PDF method. Therefore, the inconsistency among bricks in the module is also an important factor affecting the accuracy of module SOH model.

In the MFD model, the voltage data of all cells in a module at a certain moment in the fully charged terminal only needs to be collected, and the MFD value of the module at this moment can be counted by the discrete Fréchet distance method. The advantage of the MFD model is that it only needs less voltage data and there is no anthropic factor in the process of data processing, while its disadvantage is that it is necessary to collect the voltage of all cells in a module and the linear relationship between MFD and SOH is poor at the end of discharge. This is the reason why the SOH_{MFD} model at the discharge

end is not discussed in this paper. Despite this, the merit of the SOH_{MFD} model, outweighing its flaws, is that it has the highest evaluation accuracy in all the five models. EVs at home are often charged at a low current rate for a long time at night until they are full. This may be one of the best scenarios for the application of the SOH_{MFD} model.

4. CONCLUSIONS

ICA, PDF, and discrete Fréchet distance were explored to build battery module SOH models in light of charge–discharge curves of capacity calibration of a 15P4S module in an aging process. The conclusions are drawn as follows:

(1) Module SOH evaluation models by the PDF method have an obvious improvement on the basis of the same current rate and voltage range. However, the *R*-squared of the SOH evaluation model in the charging process is greater than that in the discharging process.

(2) A new SOH evaluation algorithm based on discrete Fréchet distance was proposed for the battery module, and the concept of MFD is regarded as a quick evaluation index of module SOH. There is a good linear negative correlation between MFD and module SOH. The *R*-squared of the MFD-SOH model at the end of full charge (the 0th minute) was 0.9939.

(3) A quick evaluation model for battery module SOH was proposed using the discrete Fréchet distance method, which is more accurate than those obtained from ICA and PDF methods. The reason is that the former considers the influence of the inconsistency between batteries in the module on the module SOH models. This method can be used for on-line SOH evaluation of EV battery modules because EVs at home are often charged at a low current rate for a long time at night until they are full.

CREDIT AUTHOR STATEMENT

Huiqin Sun: conceptualization, methodology, data processing, data visualization, writing (original draft). Wei Liu: conceptualization, data analysis, mechanism analysis. Zhichao Du: resources, project administration. Xinzhou Li, Zaiguo Fu: investigation, data analysis. Qiangqiang Liao: conceptualization, methodology, supervision, writing (review & editing).

ACKNOWLEDGEMENTS

This work was sponsored by the Science and Technology Commission of Shanghai Municipality (17DZ2282800 and 19DZ2271100), China.

CONFLICTS OF INTEREST

The authors declare no conflicts of interest.

DATA AVAILABILITY STATEMENT

Research data are not shared.

References

1. Y. Yang, E. G. Okonkwo, G. Huang, S. Xu, W. Sun and Y. He, *Energy Storage Mater*., 36 (2021)

186.
2. Y. Zhang, Y. Li, Y. Tao, J. Ye, A. Pan, X. Li, Q. Liao and Z. Wang, *Energy*, 193 (2020) 116555.
3. E. Martinez-Laserna, I. Gandiaga, E. Sarasketa-Zabala, J. Badeda, D.-I. Stroe, M. Swierczynski and A. Goikoetxea, *Renew. Sustain. Energy Rev*., 93 (2018) 701.
4. H. Rallo, L. Canals Casals, D. De La Torre, R. Reinhardt, C. Marchante and B. Amante, *J. Clean. Prod.,* 272 (2020) 122584.
5. X. Li, L. Zhang, Y. Liu, A. Pan, Q. Liao and X. Yang, *Int. J. Energy Res*., 44 (2019) 2337.
6. L. Canals Casals, M. Barbero and C. Corchero, *J. Clean. Prod*., 212 (2019) 99.
7. X. Xu, J. Mi, M. Fan, K. Yang, H. Wang, J. Liu and H. Yan, *J. Clean. Prod*., 213 (2019) 1080.
8. Q. Liao, M. Mu, S. Zhao, L. Zhang, T. Jiang, J. Ye, X. Shen and G. Zhou, *Int. J. Hydrogen Energy*, 42 (2017) 18817.
9. L. Chang, C. Wang, C. Zhang, L. Xiao, N. Cui, H. Li and J. Qiu, *J. Power Sources*, 459 (2020) 227901.
10. Y. Li, H. Sheng, Y. Cheng, D.-I. Stroe and R. Teodorescu, *Appl. Energy*, 277 (2020) 115504.
11. ISO 12405-4:2018-Electrically propelled road vehicles test specification for lithium-ion traction battery packs and systems - Part 4 Performance testing, https://www.iso.org/standard/71407.html, accessed: 2, 2021.
12. IEC 62660-1:2018-Secondary lithium-ion cells for the propulsion of electric road vehicles - Part 1 Performance testing, https://webstore.iec.ch/publication/33644, accessed: 1, 2021.
13. SAE J1798:2008-Recommended practice for performance rating of electric vehicle battery modules, https://www.sae.org/standards/content/j1798_200807, accessed: 1, 2021.
14. DB31/T817:2014-Technical specifications of performance test for smart grid energy storage batteries, http://www.shzj.gov.cn/art/2014/7/8/art_2828_2149.html, accessed: 1, 2021.
15. GB/T 31486-2015 Lithium-ion traction battery pack and system for electric vehicle, http://www.gb688.cn/bzgk/gb, accessed: 1, 2021.
16. GB/T 34015-2017 Recycling of traction battery used in electric vehicle-test of residual capacity, http://www.gb688.cn/bzgk/gb, accessed: 1, 2021.
17. D. Kamath, S. Shukla, R. Arsenault, H. C. Kim and A. Anctil, *Waste Manag*., 113 (2020) 497.
18. C. S. Dattu, A. Chaithanya, J. Jaidi, S. Panchal, M. Fowler and R. Fraser, *Appl. Therm. Eng.,* 199 (2021) 117586.
19. M. K. Tran, S. Panchal, V. Chauhan, N. Brahmbhatt, A. Mevawalla, R. Fraser and M. Fowler, *Int. J. Energy Res.*, https://doi.org/10.1002/er.7202.
20. M. K. Tran, A. DaCosta, A. Mevawalla, S. Panchal and M. Fowler, *Batteries,* 7 (2021) 51.
21. J. Duan, J. Zhao, X. Li, S. Panchal, J. Yuan, R. Fraser and M. Fowler, *Energies*, 14 (2021) 4187.
22. P. Gargh, A. Sarkar, Y. H. Lui, S. Shen, C. Hu, S. Hu, I. C. Nlebedim and P. Shrotriya, *J. Power Sources,* 485 (2021) 229360.
23. X. Wang, X. Wei and H. Dai, *J. Energy Storage*, 21 (2019) 618.
24. M. Dubarry, C. Truchot and B. Y. Liaw, *J. Power Sources*, 219 (2012) 204.
25. Y. Jiang, J. Jiang, C. Zhang, W. Zhang, Y. Gao and Q. Guo, *J. Power Sources*, 360 (2017) 180.
26. C. Weng, X. Feng, J. Sun and H. Peng, *Appl. Energy*, 180 (2016) 360.
27. X. Tang, C. Zou, K. Yao, G. Chen, B. Liu, Z. He and F. Gao, *J. Power Sources*, 396 (2018) 453.
28. I. Baghdadi, O. Briat, P. Gyan and J. M. Vinassa, *Electrochim. Acta*, 194 (2016) 461.
29. X. Feng, J. Li, M. Ouyang, L. Lu, J. Li and X. He, *J. Power Sources*, 232 (2013) 209.
30. Y. Merla, B. Wu, V. Yufit, N. P. Brandon, R. F. Martinez-Botas and G. J. Offer, *J. Power Sources*, 307 (2016) 308.
31. X. Lai, D. Qiao, Y. Zheng, M. Ouyang, X. Han and L. Zhou, *J. Clean. Prod*., 213 (2019) 776.
32. S. B. Vilsen and D.-I. Stroe, *J. Clean. Prod*., 290 (2021) 125700.
33. L. Wang, X. Zhao, L. Liu and C. Pan, *Electrochim. Acta*, 256 (2017) 81.
34. K. Buchin, T. Ophelders and B. Speckmann, *Comput. Geom. Theory Appl*., 73 (2018) 2.
35. H. Alt and M. Godau, *Int. J. Comput. Geom. Appl*., 5 (1995) 75.

36. T. Eiter and H. Mannila, Computing discrete Fréchet distance, Tech. Report CD-TR 94/64, (1994) Information Systems Department, Technical University of Vienna, Austria.
37. M. Dubarry and B. Y. Liaw, *J. Power Sources*, 194 (2009) 541.
38. M. Dubarry, B. Y. Liaw, M. S. Chen, S. S. Chyan, K. C. Han, W. T. Sie and S. H. Wu, *J. Power* Sources, 196 (2011) 3420.
39. Y. Jiang, J. Jiang, C. Zhang, W. Zhang, Y. Gao and N. Li, *J. Clean. Prod*., 205 (2018) 754.
40. S. Jiang and Z. Song, *Energies*, 14 (2021) 4833.
41. X. Lai, D. Qiao, Y. Zheng, M. Ouyang, X. Han and L. Zhou, *J. Clean. Prod*., 213 (2019) 776.
42. M.-H. Hung, C.-H. Lin, L.-C. Lee and C.-M. Wang, *J. Power Sources*, 268 (2014) 861.
43. Z. He, M. Gao, G. Ma, Y. Liu and S. Chen, *J. Power Sources*, 267 (2014) 576.
44. J. Xu, X. Mei, X. Wang, Y. Fu, Y. Zhao and J. Wang, *IEEE Trans. Ind. Electron*., 68 (2021) 6973.